J. Microbiol. Biotechnol. (2019), 29(2), 244–255
https://doi.org/10.4014/jmb.1810.10057

jmb

Crystal Structure and Functional Characterization of a Xylose Isomerase (*Pb*XI) from the Psychrophilic Soil Microorganism, *Paenibacillus* sp.

Sun-Ha Park[1†], Sunghark Kwon[2†], Chang Woo Lee[1,3†], Chang Min Kim[2], Chang Sook Jeong[1,3], Kyung-Jin Kim[4,5], Jong Wook Hong[6,7], Hak Jun Kim[8], Hyun Ho Park[2*], and Jun Hyuck Lee[1,3*]

[1]*Unit of Polar Genomics, Korea Polar Research Institute, Incheon 21990, Republic of Korea*
[2]*College of Pharmacy, Chung-Ang University, 84 Heukseok-ro, Dongjak, Seoul 06974, Republic of Korea*
[3]*Department of Polar Sciences, University of Science and Technology, Incheon 21990, Republic of Korea*
[4]*School of Life Sciences, KNU Creative BioResearch Group, Kyungpook National University, Daegu 41566, Republic of Korea*
[5]*KNU Institute for Microorganisms, Kyungpook National University, Daegu 41566, Republic of Korea*
[6]*Department of Bionanotechnology, Graduate School, Hanyang University, Seoul 04763, Republic of Korea*
[7]*Department of Bionanoengineering, Hanyang University, Kyunggi-do 15588, Republic of Korea*
[8]*Department of Chemistry, Pukyong National University, 45 Yongso-ro, Busan 48513, Republic of Korea*

Received: July 2, 2018
Revised: August 20, 2018
Accepted: September 15, 2018

First published online
December 14, 2018

*Corresponding authors
H.H.P.
Phone: +82-2-820-5930;
Fax: +82-2-820-3933;
E-mail: xrayleox@cau.ac.kr
J.H.L.
Phone: +82-32-760-5555;
Fax: +82-32-760-5509;
E-mail: junhyucklee@kopri.re.kr

†These authors contributed equally to this work.

pISSN 1017-7825, eISSN 1738-8872

Xylose isomerase (XI; E.C. 5.3.1.5) catalyzes the isomerization of xylose to xylulose, which can be used to produce bioethanol through fermentation. Therefore, XI has recently gained attention as a key catalyst in the bioenergy industry. Here, we identified, purified, and characterized a XI (*Pb*XI) from the psychrophilic soil microorganism, *Paenibacillus* sp. R4. Surprisingly, activity assay results showed that *Pb*XI is not a cold-active enzyme, but displays optimal activity at 60°C. We solved the crystal structure of *Pb*XI at 1.94-Å resolution to investigate the origin of its thermostability. The *Pb*XI structure shows a $(\beta/\alpha)_8$-barrel fold with tight tetrameric interactions and it has three divalent metal ions (CaI, CaII, and CaIII). Two metal ions (CaI and CaII) located in the active site are known to be involved in the enzymatic reaction. The third metal ion (CaIII), located near the β4-α6 loop region, was newly identified and is thought to be important for the stability of *Pb*XI. Compared with previously determined thermostable and mesophilic XI structures, the β1-α2 loop structures near the substrate binding pocket of *Pb*XI were remarkably different. Site-directed mutagenesis studies suggested that the flexible β1-α2 loop region is essential for *Pb*XI activity. Our findings provide valuable insights that can be applied in protein engineering to generate low-temperature purpose-specific XI enzymes.

Keywords: Cold-active protein, crystal structure, *Paenibacillus* species, xylose isomerase, X-ray crystallography

Introduction

The bioethanol production process involves biomass pretreatment, hydrolysis of polysaccharides, and yeast fermentation using *Saccharomyces cerevisiae* [1]. Prior to fermentation, xylose has to be converted to xylulose because *S. cerevisiae* can utilize only xylulose, but not xylose [2]. Xylose isomerase (XI) catalyzes the interconversion of xylose and xylulose. Bioconversion by XI has been used to produce usable sugars for fermentation. Thus, XI is gaining increased attention from researchers working in the bioenergy field [3–5]. To date, various XI genes have been identified from bacteria, fungi, and plants, and they are classified into two classes based on protein sequence similarities [6–12]. Class II XIs contain an extended N-terminal region and long loop insertions at three sites as compared with class I XIs [13]. To date, multiple class I XI structures have been reported, whereas only two class II

structures have been reported [14–20]. Structural studies of XIs have revealed that XI has a $(\beta/\alpha)_8$-barrel (TIM barrel) fold and it forms a tight tetramer. The $(\beta/\alpha)_8$-barrel structure is characterized by eight central β-strands and eight surrounding a-helices. Recently, class II XI structures from two microorganisms (*Bacteroides thetaiotaomicron* and *Piromyces* sp. E2) have been determined [11, 21, 22]. Comparative structural analysis of *B. thetaiotaomicron* XI (*Bt*XI) and class I XIs revealed that class II XIs, including *Bt*XI, have a different secondary structure configuration in the C-terminal region (the small a-helix region is missing in class II XIs) [21]. In a study on *Piromyces* sp. E2 XI (*Pi*XI), the authors investigated the divalent metal preference of *Pi*XI and determined 12 crystal structures with different metal ions and substrate combinations. The results showed that *Pi*XI has maximum activity in the presence of Mn ion and the metal-binding sites were slightly different according to the type of metal ion bound. It was suggested that the different metal-binding sites may result in variable *Pi*XI activity, depending on the metal type bound [22]. The catalytic mechanism of XI has been investigated using structural studies and computational simulations, and the reaction occurs in three steps: ring opening; hydrogen transfer between C2 and C1; and ring closure [23]. All three steps require two divalent metal ions that function as an electrophilic center to promote hydrogen transfer. Previous studies have suggested that slightly different metal ion positions are important and are highly correlated with each step of the catalytic reaction [14, 22].

Our research group has focused on finding commercially useful cold-active enzymes from psychrophilic organisms. Cold-active enzymes have catalytic activity at low and moderate temperatures compared with mesophilic homologous proteins. Recent studies have revealed that the origin of low-temperature activity is not localized in the active site, but is found in the outer regions of the protein. The cold-active enzyme has a higher degree of flexibility and softness, with reduced interactions in its outer region, whereas the active-site residues are highly conserved with mesophilic and thermophilic homologs [24, 25]. For several industrial applications, cold-active enzymes may provide economic advantages by reducing the reaction temperature [26–28]. Although several crystal structures of XIs have been solved, no information is available on the three-dimensional structures of XIs from psychrophilic organisms. Recently, we identified and purified a cold-adapted XI (*Pb*XI) from the psychrophilic soil microorganism, *Paenibacillus* sp. R4. The genome of the strain was analyzed and several putative sugar isomerase family genes were annotated by similarity searches against sequence databases. Here, we report detailed kinetic and structural analyses of *Pb*XI. Activity assay data showed that *Pb*XI displays optimal activity at 60°C, despite the fact that *Paenibacillus* sp. live in cold habitats. In addition, comparative structural analysis revealed that *Pb*XI has a different β1-α2 loop conformation that may change ligand-binding site flexibility. Our results provide useful insights for protein engineering and application of this enzyme.

Material and Methods

Cloning, Expression, and Purification of *Pb*XI

The psychrophilic soil microorganism, *Paenibacillus* sp. R4, was isolated from an active layer soil sample taken in Council, Alaska (64° 36′ 24.84′′ N, 163° 25′ 31.1′′ W). The DNA sequence of the *XI* gene was obtained by annotation of the draft genome sequence using the RAST (Rapid Annotation using Subsystem Technology) server [29]. The *XI* gene was amplified by PCR using genomic DNA of *Paenibacillus* sp. R4 as a template and the following primers with NdeI and XhoI restriction sites: forward primer, 5′-CTGCCATATGGGCTATTTTGATCATGTAGG-3′; reverse primer, 5′-CTGGCTCGAGTTATACGTTAATGATGTATT-3′. The PCR products were cloned into a pET28a expression vector (Novagen, USA) using the NdeI and XhoI restriction sites. The resultant plasmid was confirmed by DNA sequencing and was transformed into *E. coli* BL21 (DE3) for protein expression. All PbXI mutants were generated by site-directed mutagenesis using mutagenic primers (Table 1). The plasmid for wild-type PbXI was used as the template for subsequent PCRs. All PCR products were subjected to DpnI digestion to eliminate remaining template plasmids. To generate a G44A/G67P double mutant, the G44A mutant plasmid was used as a template, and primers for G67P mutation were utilized. After transformation into *E. coli* DH5α cells, the desired mutants were verified by DNA sequencing. Wild-type *Pb*XI and mutant proteins were expressed and purified using the same procedures. The cells were inoculated in 2 L of Luria-Bertani medium containing kanamycin (50 μg/ml) and were grown at 37°C to an optical density at 600 nm of 0.6–0.8. Protein expression was induced by the addition of 0.4 mM isopropyl-1-thio-β-D-galactopyranoside. After overnight incubation at 25°C, the cells were harvested by centrifugation. Lysis buffer (50 mM sodium phosphate, 300 mM NaCl, 5 mM imidazole pH 8.0) was added and the cells were sonicated on ice. After centrifugation of the disrupted cell suspension at 16,000 rpm for 1 h at 4°C, the supernatant was collected and applied on a Ni-NTA column (Qiagen, Germany) according to the manufacturer's instructions with slight modification. Briefly, following washing with 50 mM sodium phosphate buffer containing 300 mM NaCl and 20 mM imidazole (pH 8.0), purified proteins were eluted with 300 mM imidazole buffer. The eluate was concentrated using an Amicon Ultra Centrifugal Filter (Ultracel-10K; Germany). After cleavage

Table 1. Primers used for mutagenesis.

Primer	Direction	Sequence (5′ → 3′)
*Pb*XI_G44A mutant	Forward	GCATCTGCGCTTTGCTGTGGCTTACTGGC
*Pb*XI_G44A mutant	Reverse	GCCAGTAAGCCACAGCAAAGCGCAGATGC
*Pb*XI_G67P mutant	Forward	GCAGGTACTGCTCTGCGGCCATGGAACGAATTATCAGG
*Pb*XI_G67P mutant	Reverse	CCTGATAATTCGTTCCATGGCCGCAGAGCAGTACCTGC
*Pb*XI_H99A mutant	Forward	GTCGATTATTTCTGCTTCGCTGACCGTGATATCGCAC
*Pb*XI_H99A mutant	Reverse	GTGCGATATCACGGTCAGCGAAGCAGAAATAATCGAC
*Pb*XI_F143A mutant	Forward	GAATACAGCCAACATGGCCACCAATCCACGCTTCG
*Pb*XI_F143A mutant	Reverse	CGAAGCGTGGATTGGTGGCCATGTTGGCTGTATTC
*Pb*XI_W186A mutant	Forward	GCGGAAAACTACGTATTCGCAGGCGGCCGTGAGGGCTATG
*Pb*XI_W186A mutant	Reverse	CATAGCCCTCACGGCCGCCTGCGAATACGTAGTTTTCCGC
*Pb*XI_E203A mutant	Forward	CACGGACCTTGGCCTGGCACTCGATAATCTGGCAC
*Pb*XI_E203A mutant	Reverse	GTGCCAGATTATCGAGTGCCAGGCCAAGGTCCGTG

of the His-tag with thrombin, the proteins were further purified on a Superdex 200 column (GE Healthcare, USA) in 20 mM Tris-HCl buffer (pH 8.0) containing 150 mM NaCl. The purity of *Pb*XI was analyzed by 10% sodium dodecyl sulfate polyacrylamide gel electrophoresis and Coomassie staining. *Pi*XI was cloned as described previously [11], and the recombinant protein was expressed and purified using the same protocols described above for *Pb*XI.

Activity Assay

XI activity was measured by a coupled assay using D-sorbitol dehydrogenase (SDH) from sheep liver (Roche, USA) and NADH, as previously reported [11], with minor modifications. The standard 0.5-ml reaction mixture was composed of 100 mM Tris-HCl buffer (pH 8.0), 1 mM $MnCl_2$, 1 unit SDH, 0.15 mM NADH, 150 mM D-xylose, and an appropriate amount of the XI enzyme (0.25–2.5 μg). After 5 min of preincubation of the sample at 25°C, the reaction was started. The decrease in absorbance of NADH at 340 nm was measured for 3 min with a Shimadzu UV-1800 spectrophotometer (absorption coefficient of 6,220 M^{-1} cm^{-1}). The kinetic analysis was carried out under the standard assay condition, in which D-xylose concentrations were varied from 10 to 1,000 mM. The reaction rates were determined by fitting the data to the Michaelis-Menten equation by nonlinear regression. Temperature-dependent activity was examined under the standard assay condition, varying the temperature from 10°C to 70°C. SDH was active up to 60°C, and the activity decreased at 70°C. Thus, the amount of the SDH was doubled at 70°C to balance the temperature effect on enzyme activity. The assays were performed in triplicate.

Crystallization and X-Ray Diffraction Data Collection

Crystals of *Pb*XI were obtained by the sitting-drop vapor-diffusion method, using commercially available screening kits, such as the MCSG-1–4 series (Microlytic, USA) and Index and SaltRX (Hampton Research, USA), at 20°C. For crystallization, 200 nL of *Pb*XI protein solution (39 mg/ml) was mixed with 200 nL of a reservoir solution. Initial crystals appeared from several conditions within 1–2 days. These conditions were further optimized by varying the pH and the amount of precipitant. The best crystals of *Pb*XI were obtained in 0.2 M calcium chloride, 0.1 M HEPES-NaOH, pH 7.5, 27% (v/v) polypropylene glycol P400, using the sitting-drop vapor-diffusion method in 24-well plates. The crystal was directly loop-mounted and flash-cooled in liquid nitrogen. A dataset containing 360 images per 1° oscillation was collected at Pohang Accelerator Laboratory (PAL, Korea) using beam line BL-5C. Diffraction data were indexed, integrated, and scaled using *HKL-2000* [30]. Detailed data collection statistics are summarized in Table 2.

Structure Determination and Refinement

The structure of *Pb*XI was solved by the molecular replacement method, using MOLREP in the CCP4i suite [31, 32]. The crystal structure of XI from *Thermoanaerobacterium thermosulfurignes* (Protein Data Bank (PDB) code: 1A0C; not yet published), which shows 68% sequence identity with *Pb*XI, was used as a template model for molecular replacement. Repeated model building and refinement were conducted using the initial model using the programs Coot and REFMAC5, respectively [33, 34]. The final model of *Pb*XI had an R_{work} value of 20.5% and an R_{free} value of 24.9%. Model quality was checked with MolProbity [35]. Detailed refinement statistics are presented in Table 2. Atomic coordinates and structure factors have been deposited in the PDB under accession numbers 6INT.

Circular Dichroism

Circular dichroism (CD) spectra were obtained using a Chirascan Circular Dichroism Spectropolarimeter (Applied Photophysics, UK) equipped with a temperature control system. Samples were placed in a quartz cuvette with a 0.1-cm path length. The CD

Table 2. X-ray diffraction data and refinement statistics.

Data set	*Pb*XI
X-ray source	PAL-5C beam line
Space group	$P2_12_12_1$
Unit-cell parameters (Å, °)	a=89.3, b=124.0, c=315.0, α=β=γ=90.0
Wavelength (Å)	0.9796
Resolution (Å)	50.00–1.94 (1.98–1.94)
Total reflections	3,509,828
Unique reflections	236,014 (12,667)
Average I/σ (I)	42.9 (12.6)
R_{merge} [a]	0.128 (0.350)
Redundancy	13.7 (14.2)
Completeness (%)	99.8 (100.0)
Refinement	
Resolution range (Å)	23.83–1.94 (1.96–1.94)
No. of reflections of working set	254,307 (4034)
No. of reflections of test set	12,775 (349)
No. of amino acid residues	3,302
No. of water molecules	2,411
R_{cryst} [b]	0.205 (0.244)
R_{free} [c]	0.249 (0.321)
R.m.s. bond length (Å)	0.007
R.m.s. bond angle (°)	0.812
Average B value (Å^2) (protein)	19.7
Average B value (Å^2) (solvent)	26.5

[a] $R_{merge} = \Sigma |<I> - I| / \Sigma <I>$.

[b] $R_{cryst} = \Sigma ||Fo| - |Fc|| / \Sigma |Fo|$.

[c] R_{free} calculated with 5% of all reflections excluded from refinement stages using high-resolution data.

Values in parentheses refer to the highest resolution shells.

spectra were collected in the far-UV region (200–250 nm) with a 1-nm bandwidth and 0.1-nm intervals over a temperature range of 5–95°C. Data were collected in triplicate and the baseline was subtracted from the average spectra of the sample. To obtain a thermal denaturation curve, thermal changes in CD ellipticity at 222 nm were plotted over a temperature range of 5–95°C. The denaturation temperature (T_m) was defined as the point at which 50% of the sample denatured.

Results and Discussion

*Pb*XI Structure

Recombinant *Pb*XI protein was purified as a tetramer, which was confirmed by analytical gel filtration and analytical ultracentrifugation analyses. The purified *Pb*XI was crystallized in the presence of 0.2 M calcium chloride in 0.1 M HEPES buffer (pH 7.5). In this crystal form, there are eight molecules (A to H) per asymmetric unit. The crystal structure of *Pb*XI was determined at 1.94-Å resolution. For all eight molecules, the common β1-α2 loop region (residues 48–70) could not be built because of very weak electron density. It is thought that the β1-α2 loop region of *Pb*XI is intrinsically more flexible than those of other mesophilic or thermophilic XIs. This will be discussed in detail in the next section. *Pb*XI monomer shows typical characteristics of a $(\beta/\alpha)_8$-barrel (TIM barrel) structure, with protruding C-terminal helical regions (α13-α16) (Fig. 1A). The cylindrical $(\beta/\alpha)_8$-barrel structure of *Pb*XI is formed by eight central β-strands (β1-β8) that are surrounded by twelve α-helices (α1-α12). Sequence alignment of *Pb*XI with homologs indicated that *Pb*XI has a sequence typical of class II XIs (Fig. 1B). The core of the central β-barrel is the active site, which is occluded by two metal ions coordinated by negatively charged residues (Glu230, Glu266, Asp294, Asp305, Asp307, and Asp338) and bulky hydrophobic side chains, such as Trp137, Phe143, and Trp186. The dimer interface of *Pb*XI is formed mainly by the α7 and α10 helices, and the buried molecular surface area is approximately 4,107.25 Å^2/subunit. The tetramer interface is mainly formed by the α12 and α16 helices and the β7-α11 loop region, and the buried molecular surface area is approximately 2,718.825 Å^2/subunit (Fig. 2A). Each buried surface area was calculated using the program *ArealMol* in *CCP4i* [32]. We observed strong electron density for two metal ions (CaI and CaII) in the active site and one metal ion (CaIII) near the β4-α6 loop region of each subunit. CaI and CaII were located at the same well-defined locations as in other XIs. On the other hand, CaIII was newly detected (Fig. 2B). Initially, we identified strong electron density near the subunit interaction region during *Pb*XI structure refinement. Since 0.2 M $CaCl_2$ buffer was used for *Pb*XI crystallization, the third metal-binding site was modeled using calcium ion (CaIII). Refined CaIII ion fit well into the electron density map and it had full occupancy (1.0) and an average B-factor value of 14.42 from all chains. In detail, CaIII is coordinated by the side chain of Glu203 and the main-chain O atom of Gly191. Furthermore, CaIII interacts with side chains of Thr154 and Thr198 and the main-chain O atom of His150 via water molecules. The residues Tyr386 and Arg385 from the other subunit of the dimer are also involved in water-mediated CaIII interactions. It is thought that CaIII might contribute to structural stabilization of the dimer. In addition, the CaIII ion forms a regular hepta coordination with Tyr386,

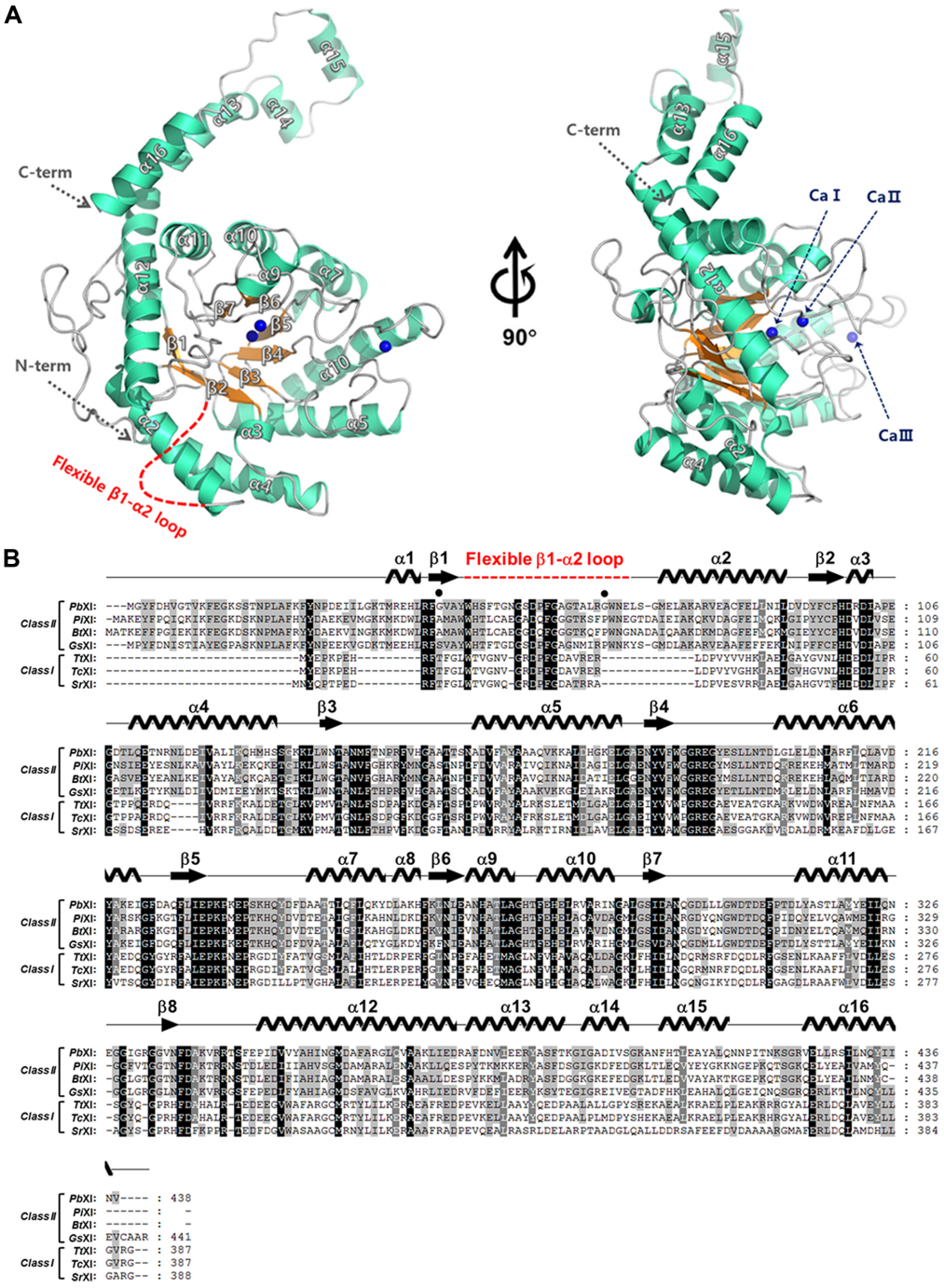

Fig. 1. Crystal structure of *Pb*XI and multiple amino acid sequence alignment of XI proteins.
(**A**) Ribbon diagram of *Pb*XI monomer showing the secondary structure elements and three bound calcium ions. The flexible β1-α2 loop region (dotted red line) is not included in the atomic model because of very weak electron density. (**B**) Multiple sequence alignment of *Pb*XI, *Pi*XI (*Piromyces* sp.; UniProtKB code: Q9P8C9), *Bt*XI (*Bacteroides thetaiotaomicron*; UniProtKB code: Q8A9M2), *Gs*XI (*Geobacillus stearothermophilus*; UniProtKB code: P54273), *Tt*XI (*Thermus thermophilus*; UniProtKB code: P26997), *Tc*XI (*Thermus caldophilus*; UniProtKB code: P56681), and *Sr*XI (*Streptomyces rubiginosus*; UniProtKB code: P24300). Strictly and partially conserved residues are shaded black and gray, respectively. Two glycine residues (Gly44 and Gly67) thought to be critical for the flexibility of the β1-α2 loop region in *Pb*XI are indicated by black circles. Secondary structures obtained from the crystal structure of *Pb*XI are shown above the aligned sequence. Multiple sequence alignment was conducted with ClustalX and was edited with GeneDoc.

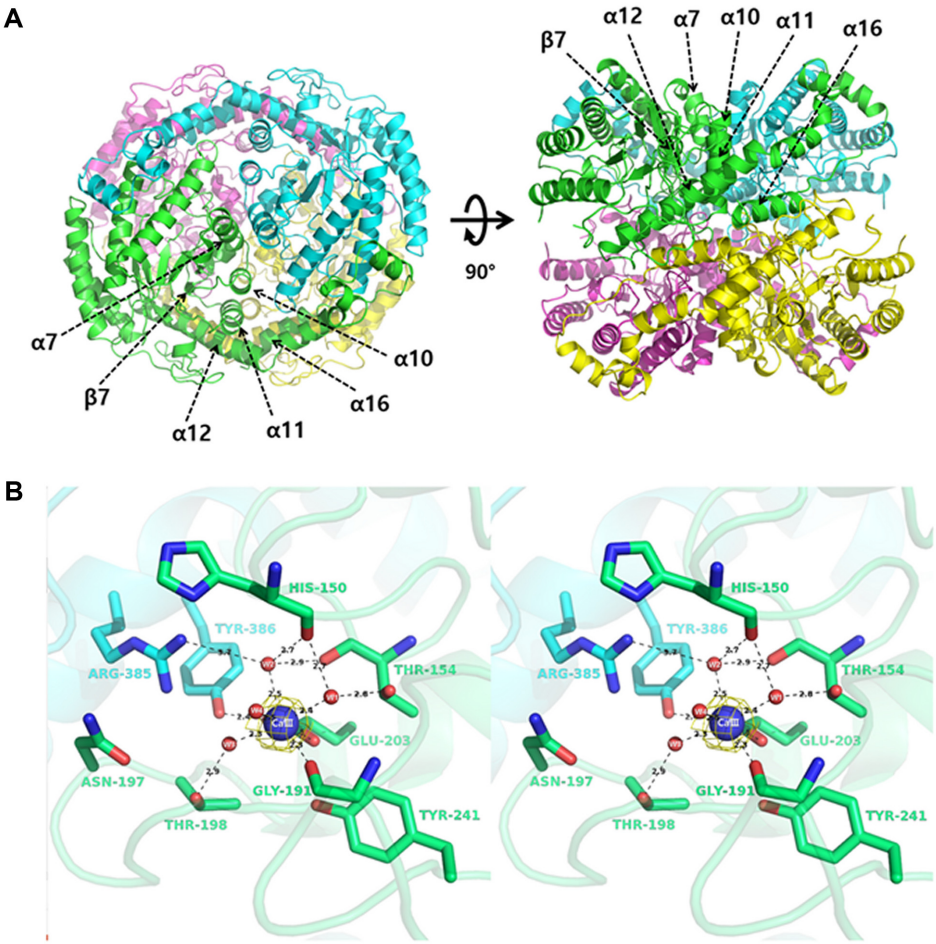

Fig. 2. Oligomeric state and CaIII binding site of *Pb*XI.
(**A**) Cartoon model of the tetrameric conformation of *Pb*XI. Each subunit is indicated in a different color. The regions involved in dimer and tetramer interfaces are indicated by black arrows. (**B**) A stereo view of the CaIII-binding site in *Pb*XI. Bound calcium ion is represented by a blue sphere. 2Fo-Fc map of the CaIII contoured at the 1-δ level. The electron density is indicated in yellow. Water molecules tightly interacting with the calcium ion are represented by red spheres. Interaction residues of the subunit A are represented by limegreen sticks. Interaction residues of the subunit B are represented by cyan sticks.

Glu203, Gly191, and three water molecules. Notably, these three residues are strictly conserved in class II XIs. This means that the third metal-binding site may be important for the biological function of class II XIs. Based on these data alone, we could not rule out the possibility that another divalent metal ion was bound in the third metal-binding site. Further studies are needed to fully identify the metal ion. We considered the third metal ion a putative CaIII in this study. Structure alignments using the Dali server [36] indicated that *Pb*XI has the highest structural similarity with XI from *Thermotoga neapolitana* (PDB code: 1a0e), with a Z-score of 58.1. In addition, XI from *Geobacillus stearothermophilus* (PDB code: 1a0d), XI from *Piromyces* sp. E2 (PDB code: 5nhm), and XI from *Bacteroides thetaiotaomicron* (PDB code: 4xkm) showed high structural similarity (Table 3) [21, 22].

Active Site of *Pb*XI

*Pb*XI has a negatively charged substrate-binding site, and two calcium ions (CaI and CaII) are tightly bound to that site (Fig. 3A). Comparison and structural superposition of XIs revealed a striking difference in the β1-α2 loop region near the active site (Fig. 3B). As mentioned above, *Pb*XI has no β1-α2 loop region residues in its structural model because of very weak electron density. Sequence alignment results indicated that *Pb*XI contains two Gly residues (Gly44 and Gly67) at the front and rear positions of the β1-α2 loop (Fig. 3C). Notably, these two Gly residues are not

Table 3. Structural homologs of *Pb*XI according to a search against the DALI-Lite server.

Protein	PDB code	DALI score	UniProtKB code	Sequence % ID with *Pb*XI (Aligned residue number/ Total residue number)	Reference
XI from *Thermotoga neapolitana*	1A0E	58.1	P45687	63% (412/443)	Not yet published
XI from *Geobacillus stearothermophilus*	1A0D	56.9	P54273	72% (412/437)	Not yet published
XI from *Piromyces* sp. (strain E2)	5NHM	56.2	Q9P8C9	50% (409/436)	[22]
XI from *Bacteroides thetaiotaomicron*	4XkM	56.1	Q8A9M2	51% (409/435)	[21]
XI from *Thermoanaerobacterium thermosulfurigenes*	1A0C	55.6	P19148	69% (411/437)	Not yet published
XI from *Thermus thermophilus*	1BXB	38.5	P26997	28% (357/387)	[15]
XI from *Streptomyces rubiginosus*	5AVN	38.3	P24300	26% (356/387)	[40]
XI from *Streptomyces olivochromogenes*	1XYB	38.2	P15587	26% (357/386)	[41]
XI from *Thermus caldophilus*	1BXC	38.0	P56681	27% (357/387)	[15]
XI from *Streptomyces diastaticus*	1QT1	38.0	P50910	26% (357/387)	[42]

present in thermophilic or mesophilic homologs, which have Pro, Ala, or Ser in the corresponding position. Thus, we suggest that these two Gly residues may increase the flexibility of the β1-α2 loop and are important for the

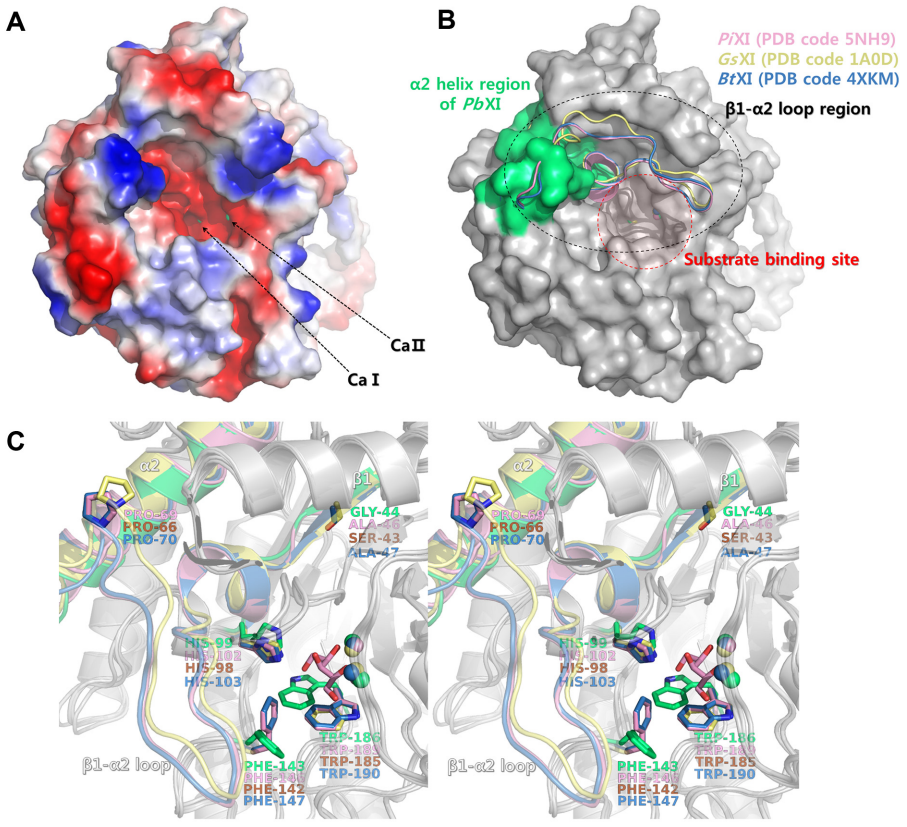

Fig. 3. Structural comparison of *Pb*XI, *Pi*XI, *Gs*XI, and *Bt*XI.
(**A**) Electrostatic surface charge representation of the substrate-binding pocket in *Pb*XI. The CaI and CaII metal ions are located in the negatively charged substrate-binding pocket. (**B**) The β1-α2 loop is located near the substrate-binding site and thus, this region is thought to have a gatekeeper function in substrate entry and product release. In the *Pb*XI structure, the β1-α2 loop region is more flexible and this characteristic may be important for its higher activity. (**C**) Stereodiagram of superimposed substrate-binding sites in *Pb*XI, *Pi*XI, *Gs*XI, and *Bt*XI structures. Notably, unliganded PbXI has different conformations of His99, Phe143, and Trp186 residues.

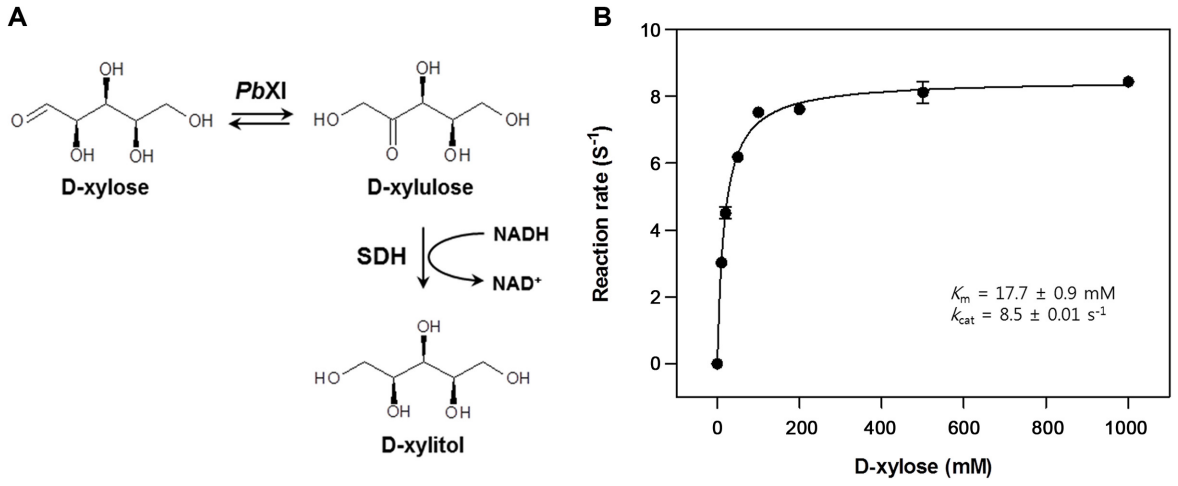

Fig. 4. Kinetics of *Pb*XI.
(**A**) XI reaction catalyzed by *Pb*XI. (**B**) Michaelis-Menten plot of the kinetics of *Pb*XI. Isomerase activity was measured spectrophotometrically by a coupled reaction with D-sorbitol dehydrogenase (SDH). The reaction rates were measured in the presence of varying concentrations of D-xylose.

activity of *Pb*XI. Another notable feature of the active site is the conformational changes of Phe143 and Trp186, which have rotational movement in *Pb*XI. The aromatic ring of Trp189 (corresponding to Trp186 in *Pb*XI) in xylose (linear form)-bound *Pi*XI (PDB code: 5NH9) has a hydrophobic stacking interaction with the carbon backbone of xylose [22]. In the *Pi*XI structure, the aromatic ring of Phe146 (corresponding to Phe143 in *Pb*XI) also contributes to the formation of the hydrophobic sugar-binding pocket. In the *Pb*XI structure, these two residues have different conformations. Probably, the conformational changes of these two residues are associated with the movement of the β1-α2 loop region. In the *Pi*XI structure, the movement of Phe146 and Trp189 might be induced by the binding of ligand, which may further induce the closure of the β1-α2 loop. The β1-α2 loop may have a gatekeeper function to control substrate entry and product release through open- and close-state conformations. In the *Pb*XI structure, this gate is more flexible and it may be important for its activity. This hypothesis was confirmed by site-directed mutagenesis studies and has led to the suggestion that the elevated flexibility of the β1-α2 loop region is crucial for *Pb*XI activity.

Activity Assay and Functional Analysis of *Pb*XI

*Pb*XI activity was assayed by a coupled enzyme assay in which D-xylose is converted to D-xylulose by XI activity and D-xylulose is reduced to xylitol via NADH oxidation by SDH. XIs require divalent metal cations for stability and activity, and their metal preference depends on the nature of the substrate and on the XI class [37]. Amino acid sequence alignment indicated that *Pb*XI belongs to class II. Previous studies have shown that class II XIs, including *Pi*XI, prefer Mn^{2+} for activity on xylose [11, 22]. Thus, kinetic parameters of *Pb*XI for D-xylose were determined in the presence of 1 mM $MnCl_2$ with varying D-xylose concentrations (10–1000 mM) (Fig. 4 and Table 4). A k_{cat} of 8.5 s^{-1} and a K_m of 17.7 mM were obtained for the isomerase reactions at 25°C, which is comparable to kinetics data for *Pi*XI (Table 4) [22]. The two *Pi*XI enzymes shown in Table 4

Table 4. Comparison of kinetic parameters of Class II XIs, *Pb*XI, and *Pi*XI[a].

Origin	Xylose			Temperature	Reference
	K_m (mM)	k_{cat} (s^{-1})	k_{cat}/K_m ($s^{-1}M^{-1}$)		
Paenibacillus sp.	17.7	8.5	480	25°C	This study
Piromyces sp. E2	4.3	4.5	1100	30°C	[22]
Piromyces sp. E2	16.5	27.1	1600	30°C	[11]

[a]Activities for conversion of xylose to xylulose were determined in the presence of 1 mM Mn ion.

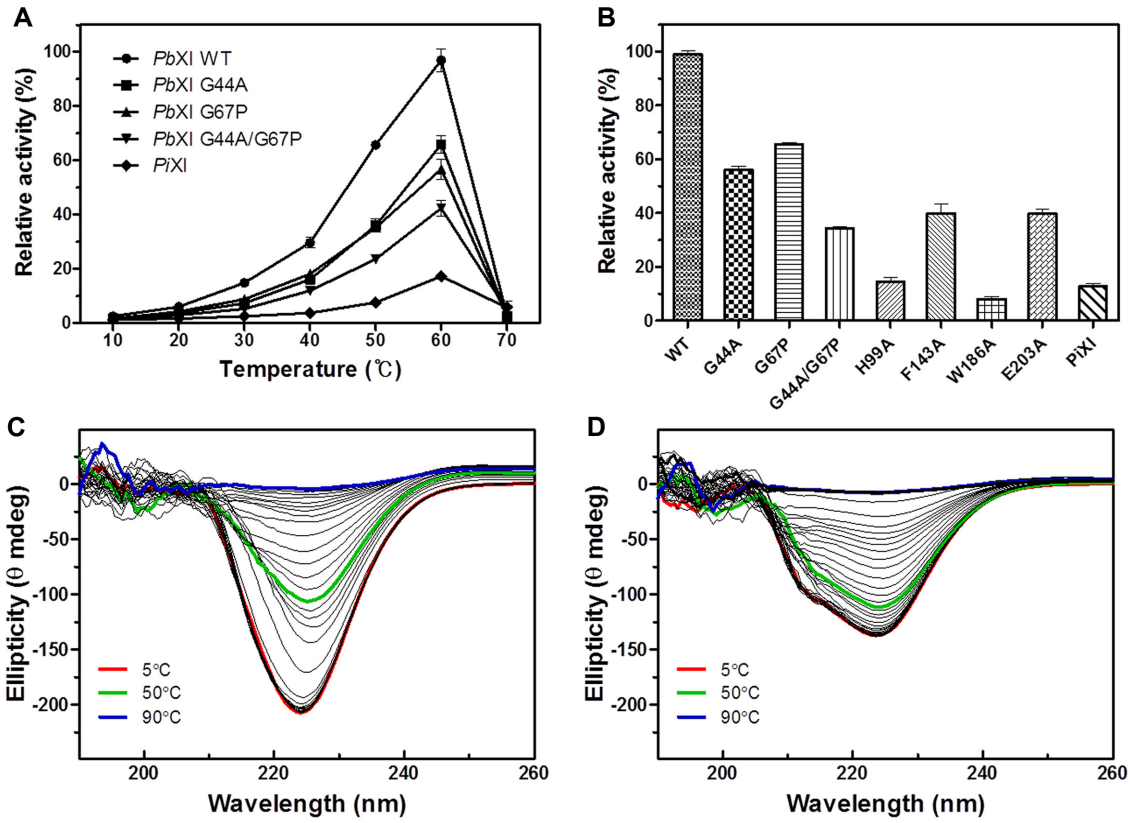

Fig. 5. Biochemical characterization of *Pb*XI.

(**A**) Effect of reaction temperature on *Pb*XI activity. Isomerase activities of the enzymes were evaluated in the temperature range of 10–70°C. Enzymatic activity is expressed as a percentage of the maximum activity (100%). (**B**) Specific activities for isomerization of D-xylose catalyzed by wild-type *Pb*XI and mutant enzymes, and *Pi*XI. The reactions were carried out at 25°C under standard assay conditions. Circular dichroism (CD) spectra during thermal denaturation of wild-type *Pb*XI (**C**) and the E203A mutant (**D**). CD spectra were measured over a temperature range of 5–95°C in the far-UV region (200–250 nm) with 1-nm bandwidth.

exhibited considerably different kinetics. This is probably due to the fact that experimental conditions, including buffer pH and substrate concentrations, were different. In addition, the position of the His-tag at the N- or C-terminus in the *Pi*XIs may affect the enzyme kinetics.

Next, the temperature dependence of *Pb*XI activity was investigated. *Pb*XI showed an increase in activity with increasing temperature and was optimally active at 60°C. However, at a temperature above 60°C, *Pb*XI was rapidly inactivated (Fig. 5A). Comparative structural analysis and amino acid sequence alignment showed that *Pb*XI has a remarkably different β1-α2 loop conformation and contains two Gly residues (Gly44 and Gly67) in this loop. Thus, we mutated these two Gly residues in *Pb*XI to Ala or Pro, which are the corresponding residues in thermophilic or mesophilic homologs. Two single mutants (G44A and G67P) and one double mutant (G44A/G67P) were constructed, and their XI activities on xylose were measured at different reaction temperatures (Figs. 5A and 5B). Compared to the wild type, all mutants showed significantly reduced activities at all tested reaction temperatures, and in particular, G44A/G67P had strongly reduced activity. It can thus be suggested that these two Gly residues may play roles in enhancing the catalytic activity of *Pb*XI by increasing the flexibility of the β1-α2 loop near the substrate binding site. To verify the hypothesis that the conformational changes of Phe143 and Trp186 in the active site of *Pb*XI are important for substrate binding, we also constructed Ala mutants, F143A and W186A, which both showed significantly reduced activity. As expected, the catalytic residue mutant (H99A) showed an approximately 90% reduction in activity. To investigate the role of the CaIII metal ion in *Pb*XI, an E203A mutant was constructed, as the Glu203 residue is involved in CaIII binding. Notably, the E203A

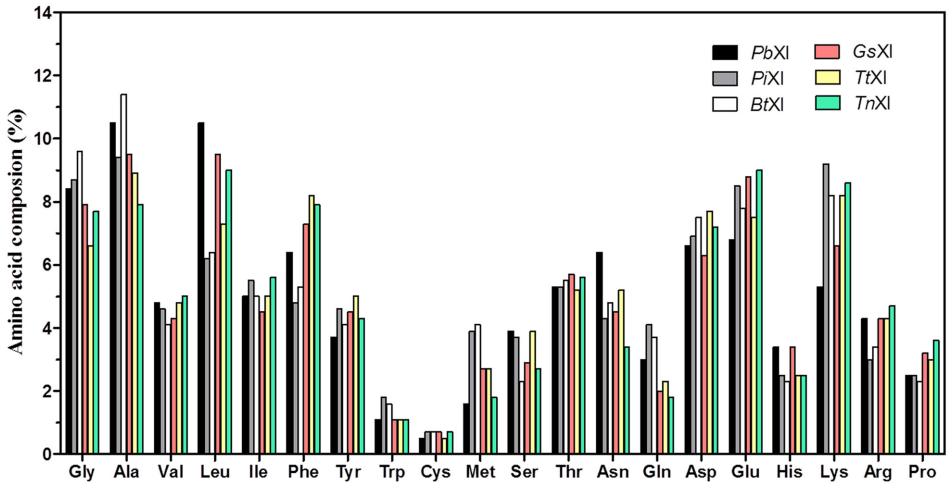

Fig. 6. Total amino acid composition of class II XIs.

The content of each amino acid is expressed as a percentage of total amino acid content of the protein. *Pi*XI; from *Piromyces* sp. E2, *Bt*XI; from *Bacteroides thetaiotaomicron*, *Gs*XI; from *Geobacillus stearothermophilus*, TtXI; from *Thermoanaerobacterium thermosulfurigenes*, TnXI; from *Thermotoga neapolitana*.

mutant also showed a 50% reduction in activity. This result indicated that CaIII binding may be important for the stability and/or activity of *Pb*XI. In addition, it should be noted that *Pb*XI has ten-fold higher activity than *Pi*XI at 25°C (Figs. 5A and 5B), presumably because of the flexibility of the β1-α2 loop region of *Pb*XI. According to previous reports [11, 22], the catalytic efficiencies (k_{cat}/K_m) of *Pi*XIs are higher than that of *Pb*XI (Table 4). However, in this study, we newly purified *Pi*XI and compared the activity of *Pi*XI with that of *Pb*XI using 150 mM D-xylose as a substrate in the same assay condition.

*Pb*XI stability was determined by thermal denaturation using far-UV CD spectroscopy; T_m was 51.1°C (Fig. 5C). To better understand the biological role of the third metal ion, we examined CD spectra of an E203A mutant in comparison with spectra of the wild type. The activity of the E203A mutant was significantly lower than that of the wild-type protein (Fig. 5B). The Glu203 residue is involved in putative CaIII ion coordination. Replacement of the glutamate residue with an alanine residue is expected to disturb putative metal binding in *Pb*XI. There was a significant difference between the CD spectrum of wild-type *Pb*XI and that of the E203A mutant, although the overall T_m of the E203A mutant was similar to that of wild-type *Pb*XI (Figs. 5C and 5D). This means that the third metal ion does not affect the secondary structure stability of *Pb*XI. Alternatively, the alanine substitution of Glu203 might have resulted in a local conformational change. Further, lack of the third metal ion may have weakened subunit-subunit interactions because the third metal ion is located in the subunit-subunit interface. The reduced interaction among subunits may have resulted in reduced *Pb*XI activity. The identification of a novel metal-binding site and biochemical analyses in this study may pave the way toward an understanding of the relationship between subunit-subunit stability and the activity of class II XIs.

Enzymes from psychrophiles generally have a low optimum temperature and are heat labile; however, *Pb*XI is moderately thermophilic. Notably, *Pb*XI has high amino acid sequence identity to class II XIs from two thermophiles, *Tt*XI from *Thermoanaerobacterium thermosufurigenes* (68% sequence identity) and *Tn*XI from *Thermotoga neapolitana* (63% sequence identity), but has a considerably low optimum temperature [38, 39]. *Tt*XI and *Tn*XI have very high amino acid sequence identity (70.4%), but *Tn*XI is more thermostable than *Tt*XI, with optimum temperatures of 95°C for *Tn*XI and 85°C for *Tt*XI. Mutational studies indicated that two additional Pro residues of *Tn*XI (Pro58 and Pro62) play important roles in hyperthermophilic properties. The substitution to Pro can increase protein stability by decreasing the entropy of the unfolded state. To explain the differences in optimum temperature between class II XIs, we analyzed total amino acid compositions. As shown in Fig. 6, there is a clear correlation between the Asn+Gln content and the growth temperature of the source organism, and *Pb*XI has the highest Asn+Gln content among

XIs from mesophilic, thermophilic, and hyperthermophilic organisms. Moreover, the lower amount of Pro residues in *Pb*XI might explain its thermal properties.

In conclusion, we reported the first crystal structure of a XI from the psychrophilic soil microorganism, *Paenibacillus* sp. R4. Sequence alignment and structural and biochemical analyses provided novel insights into the factors that determine the activity of *Pb*XI. Our findings suggest that site-directed mutagenesis with the aim of increasing the flexibility near the substrate-binding region may offer an alternative strategy for rational design of low-temperature purpose-specific XI enzymes.

Acknowledgments

The authors thank the staff at the X-ray crystallography core facility of the Korea Basic Science Institute (Ochang, Korea) and BL-5C of the Pohang Accelerator Laboratory (Pohang, Korea) for assistance with data collection. This work was supported by the Korea Polar Research Institute (grant no. PE19210 to J.H.L.). Additional support was provided by the Basic Science Research Program 2018R1A2B6005354 through the National Research Foundation of Korea (NRF) funded by the Ministry of Science, ICT and Future Planning of Korea.

Conflict of Interest

The authors have no financial conflicts of interest to declare.

References

1. Mosier N, Wyman C, Dale B, Elander R, Lee Y, Holtzapple M, *et al.* 2005. Features of promising technologies for pretreatment of lignocellulosic biomass. *Bioresour. Technol.* **96:** 673-686.
2. Chiang L-C, Gong C-S, Chen L-F, Tsao GT. 1981. D-Xylulose fermentation to ethanol by *Saccharomyces cerevisiae*. *Appl. Environ. Microbiol.* **42:** 284-289.
3. Chandrakant P, Bisaria V. 2000. Simultaneous bioconversion of glucose and xylose to ethanol by *Saccharomyces cerevisiae* in the presence of xylose isomerase. *Appl. Microbiol. Biotechnol.* **53:** 301-309.
4. Gong C-S, Chen L-F, Flickinger MC, Chiang L-C, Tsao GT. 1981. Production of ethanol from D-xylose by using D-xylose isomerase and yeasts. *Appl. Environ. Microbiol.* **41:** 430-436.
5. Zhou H, Cheng J-S, Wang BL, Fink GR, Stephanopoulos G. 2012. Xylose isomerase overexpression along with engineering of the pentose phosphate pathway and evolutionary engineering enable rapid xylose utilization and ethanol production by *Saccharomyces cerevisiae*. *Metabol. Eng.* **14:** 611-622.
6. Madhavan A, Tamalampudi S, Ushida K, Kanai D, Katahira S, Srivastava A, *et al.* 2009. Xylose isomerase from polycentric fungus *Orpinomyces*: gene sequencing, cloning, and expression in Saccharomyces cerevisiae for bioconversion of xylose to ethanol. *Appl. Microbiol. Biotechnol.* **82:** 1067-1068.
7. Moes CJ, Pretorius IS, van Zyl WH. 1996. Cloning and expression of the Clostridium thermosulfurogenes D-xylose isomerase gene (xylA) in *Saccharomyces cerevisiae*. *Biotechnol. Lett.* **18:** 269-274.
8. Sarthy A, McConaughy B, Lobo Z, Sundstrom J, Furlong C, Hall B. 1987. Expression of the *Escherichia coli* xylose isomerase gene in *Saccharomyces cerevisiae*. *Appl. Environ. Microbiol.* **53:** 1996-2000.
9. Kristo P, Saarelainen R, Fagerström R, Aho S, Korhola M. 1996. Protein purification, and cloning and characterization of the cDNA and gene for xylose isomerase of barley. *Eur. J. Biochem.* **237:** 240-246.
10. Umemoto Y, Shibata T, Araki T. 2012. D-xylose isomerase from a marine bacterium, *Vibrio* sp. strain XY-214, and D-xylulose production from β-1, 3-xylan. *Marine Biotechnol.* **14:** 10-20.
11. Son H, Lee S-M, Kim K-J. 2018. Crystal structure and biochemical characterization of xylose isomerase from *Piromyces* sp. E2. *J. Microbiol. Biotechnol.* **28:** 571-578.
12. Dekker K, Yamagata H, Sakaguchi K, Udaka S. 1991. Xylose (glucose) isomerase gene from the thermophile *Thermus thermophilus*: cloning, sequencing, and comparison with other thermostable xylose isomerases. *J. Bacteriol.* **173:** 3078-3083.
13. Park J-H, Batt CA. 2004. Restoration of a defective *Lactococcus lactis* xylose isomerase. *Appl. Environ. Microbiol.* **70:** 4318-4325.
14. Kovalevsky AY, Hanson L, Fisher SZ, Mustyakimov M, Mason SA, Forsyth VT, *et al.* 2010. Metal ion roles and the movement of hydrogen during reaction catalyzed by D-xylose isomerase: a joint x-ray and neutron diffraction study. *Structure* **18:** 688-699.
15. Chang C, Park BC, Lee D-S, Suh SW. 1999. Crystal structures of thermostable xylose isomerases from *Thermus caldophilus* and *Thermus thermophilus*: possible structural determinants of thermostability. *J. Mol. Biol.* **288:** 623-634.
16. Allen KN, Lavie A, Glasfeld A, Tanada TN, Gerrity DP, Carlson SC, *et al.* 1994. Role of the divalent metal ion in sugar binding, ring opening, and isomerization by D-xylose isomerase: replacement of a catalytic metal by an amino acid. *Biochemistry* **33:** 1488-1494.
17. Bae J-E, Hwang KY, Nam KH. 2018. Structural analysis of substrate recognition by glucose isomerase in Mn^{2+} binding mode at M2 site in *S. rubiginosus*. *Biochem. Biophys. Res. Commun.* **503:** 770-775.
18. Toteva MM, Silvaggi NR, Allen KN, Richard JP. 2011. Binding energy and catalysis by D-xylose isomerase: kinetic, product, and X-ray crystallographic analysis of enzyme-catalyzed isomerization of (R)-glyceraldehyde. *Biochemistry* **50:** 10170-10181.

19. Carrell H, Rubin BH, Hurley TJ, Glusker JP. 1984. X-ray crystal structure of D-xylose isomerase at 4-A resolution. *J. Biol. Chem.* **259:** 3230-3236.
20. Jenkins J, Janin J, Rey F, Chiadmi M, Van Tilbeurgh H, Lasters I, *et al.* 1992. Protein engineering of xylose (glucose) isomerase from *Actinoplanes missouriensis*. 1. Crystallography and site-directed mutagenesis of metal binding sites. *Biochemistry* **31:** 5449-5458.
21. Han B, Bong SM, Cho J, Kim M, Kim SJ, Lee BI. 2015. Crystal structure of a Class 2 D-xylose isomerase from the human intestinal tract microbe *Bacteroides thetaiotaomicron*. *Biodesign* **289:** 41-47.
22. Lee M, Rozeboom HtJ, de Waal PP, de Jong RM, Dudek HM, Janssen DB. 2017. Metal dependence of the xylose isomerase from *Piromyces* sp. E2 explored by activity profiling and protein crystallography. *Biochemistry* **56:** 5991-6005.
23. Lee C, Bagdasarian M, Meng M, Zeikus J. 1990. Catalytic mechanism of xylose (glucose) isomerase from *Clostridium thermosulfurogenes*. Characterization of the structural gene and function of active site histidine. *J. Biol. Chem.* **265:** 19082-19090.
24. Isaksen GV, Åqvist J, Brandsdal BO. 2014. Protein surface softness is the origin of enzyme cold-adaptation of trypsin. *PLoS Comput. Biol.* **10:** e1003813.
25. Papaleo E, Pasi M, Riccardi L, Sambi I, Fantucci P, Gioia LD. 2008. Protein flexibility in psychrophilic and mesophilic trypsins. Evidence of evolutionary conservation of protein dynamics in trypsin-like serine-proteases. *FEBS Lett.* **582:** 1008-1018.
26. Santiago M, Ramírez-Sarmiento CA, Zamora RA, Parra LP. 2016. Discovery, molecular mechanisms, and industrial applications of cold-active enzymes. *Front. Microbiol.* **7:** 1408.
27. Cavicchioli R, Siddiqui KS, Andrews D, Sowers KR. 2002. Low-temperature extremophiles and their applications. *Curr. Opin. Biotechnol.* **13:** 253-261.
28. Joseph B, Ramteke PW, Thomas G, Shrivastava N. 2007. Cold-active microbial lipases: a versatile tool for industrial applications. *Biotechnol. Mol. Biol. Rev.* **2:** 39-48.
29. Overbeek R, Olson R, Pusch GD, Olsen GJ, Davis JJ, Disz T, *et al.* 2013. The SEED and the Rapid Annotation of microbial genomes using Subsystems Technology (RAST). *Nucleic Acids Res.* **42:** D206-D214.
30. Otwinowski Z, Minor W. 1997. Processing of X-ray diffraction data collected in oscillation mode. *Methods Enzymol.* **276:** 307-326.
31. Vagin A, Teplyakov A. 1997. MOLREP: an automated program for molecular replacement. *J. Appl. Crystallogr.* **30:** 1022-1025.
32. Winn MD, Ballard CC, Cowtan KD, Dodson EJ, Emsley P, Evans PR, *et al.* 2011. Overview of the CCP4 suite and current developments. *Acta Crystallographica Section Biol. Crystallogr.* **67:** 235-242.
33. Emsley P, Cowtan K. 2004. Coot: model-building tools for molecular graphics. *Acta Crystallogr. D Biol. Crystallogr.* **60:** 2126-2132.
34. Murshudov GN, Skubák P, Lebedev AA, Pannu NS, Steiner RA, Nicholls RA, *et al.* 2011. REFMAC5 for the refinement of macromolecular crystal structures. *Acta Crystallogr. D Biol. Crystallogr.* **67:** 355-367.
35. Chen VB, Arendall WB, Headd JJ, Keedy DA, Immormino RM, Kapral GJ, *et al.* 2010. MolProbity: all-atom structure validation for macromolecular crystallography. *Acta Crystallogr. D Biol. Crystallogr.* **66:** 12-21.
36. Holm L, Rosenström P. 2010. Dali server: conservation mapping in 3D. *Nucleic Acids Res.* **38:** W545-W549.
37. Vieille C, Epting KL, Kelly RM, Zeikus JG. 2001. Bivalent cations and amino-acid composition contribute to the thermostability of *Bacillus licheniformis* xylose isomerase. *Eur. J. Biochem.* **268:** 6291-6301.
38. Sriprapundh D, Vieille C, Zeikus JG. 2000. Molecular determinants of xylose isomerase thermal stability and activity: analysis of thermozymes by site-directed mutagenesis. *Protein Eng.* **13:** 259-265.
39. Vieille C, Hess JM, Kelly RM, Zeikus JG. 1995. *xylA* cloning and sequencing and biochemical characterization of xylose isomerase from *Thermotoga neapolitana*. *Appl. Environ. Microbiol.* **61:** 1867-1875.
40. Sugiyama S, Maruyama M, Sazaki G, Hirose M, Adachi H, Takano K, *et al.* 2012. Growth of protein crystals in hydrogels prevents osmotic shock. *J. Am. Chem. Soc.* **134:** 5786-5789.
41. Lavie A, Allen KN, Petsko GA, Ringe D. 1994. X-ray crystallographic structures of D-xylose isomerase-substrate complexes position the substrate and provide evidence for metal movement during catalysis. *Biochemistry* **33:** 5469-5480.
42. Zhu X-Y, Teng Mk, Niu L-W, Xu C, Wang Y-Z. 2000. Structure of xylose isomerase from *Streptomyces diastaticus* No. 7 strain M1033 at 1.85 Å resolution. *Acta Crystallogr. D Biol. Crystallogr.* **56:** 129-136.